Polymer-Based Ultrasonic Motors Utilizing High-Order Vibration Modes

Jiang Wu, Yosuke Mizuno, *Senior Member, IEEE*, and Kentaro Nakamura, *Member, IEEE*

***Abstract*—Our previous studies showed that traveling-wave rotary ultrasonic motors with polymer-based vibrators yielded limited output power when operating in the commonly used low-order bending vibration modes. In this study, we employ a high-order bending mode in the polymer-based cylindrical ultrasonic motor, because this mode yields a relatively high electromechanical coupling factor, which may lead to high output power of the motor. Additionally, in contrast with the low-order modes with only vertical nodal lines, the high-order mode has both horizontal and vertical nodal lines on the circumferential outer surface of the polymer-based vibrator. With these attractive advantages, it is worth investigating basic vibration characteristics of polymer-based vibrators operating in high-order modes and their applications to ultrasonic motors. The vibrating body is made of poly phenylene sulfide, a functional polymer exhibiting low mechanical loss even under high-amplitude ultrasonic vibration and is activated by a piezoelectric ceramic element bonded on the back surface. The high-order modes are optimal for polymer-based vibrators with practical thicknesses, because their equivalent stiffnesses and masses are relatively low when operating in this mode. Polymer-based motors with the high-order modes exhibit relatively high output torques and powers, compared with not only polymer-based motors with low-order bending modes, but also metal-based motors operating in high-order vibration modes.**

***Index Terms*—Electromechanical coupling factor, high-order vibration mode, polymer, ultrasonic motor (USM).**

I. INTRODUCTION

EXHIBITING simple structures, fast response times, precise positioning capability, and high torques at low speeds [1]–[3], ultrasonic motors (USMs) have been extensively investigated in the past three decades, and practically applied to some special fields [1], [4]–[6]. USMs dominantly consist of vibrators and rotors, which are pressed to each other to effectively utilize the frictional force [5]–[9]. Vibrators are core components of USMs [1], [10]–[12]. Fig. 1(a) depicts a cylindrical vibrator, which typically comprises a piezoelectric ceramic element and a metal vibrating body [4], [9], [10]. When four voltages with 90° phase differences are applied, four flexural standing waves, $u_1 = A\sin(\omega t)\sin(k\theta)$, $u_2 = A\cos(\omega t)\cos(k\theta)$, $u_3 = -A\sin(\omega t)\sin(k\theta + \pi)$, and $u_4 = -A\cos(\omega t)\cos(k\theta + \pi)$, are excited on the vibrator. Here, A, ω, and k respectively represent the amplitude of the vertical vibration velocity, angular resonance frequency, and wave number ($k = 3$ for our motors); t and θ are the time and circumferential angle, respectively. The superposition of these standing waves forms a traveling wave

$$u_z = \sum_{i=1}^{4} u_i = 2A\cos(\omega t - k\theta). \tag{1}$$

In flexural vibration, the vibration velocity along the circumferential direction is as follows:

$$u_\theta = -\alpha \cdot \frac{\partial u_z}{\partial \theta} = -2\alpha k A \sin(\omega t - k\theta) \tag{2}$$

where α is a ratio determined by the vibration mode and structural parameters of the cylindrical vibrator [1]. Thus,

$$\left(\frac{u_z}{2A}\right)^2 + \left(\frac{u_\theta}{2\alpha k A}\right)^2 = 1 \tag{3}$$

this equation demonstrates that the points on the vibrator surface exhibit elliptical motions, which drive the rotor via frictional force. Recently, lightweight USMs have become increasingly demanded as potential key actuators in robotic applications or optical instruments [5], [6]. In previous studies, we attempted to exploit poly phenylene sulfide (PPS), a functional polymer with low mechanical loss [13]–[15], as the vibrating body to reduce the USM weight. Compared to the USMs with metal-based vibrators, PPS-based USMs had relatively high rotational speeds but limited output torques [14].

The bending mode shown in Fig. 1(b) has been employed in our previous polymer-based ring-shaped USMs, as well as in many conventional metal-based USMs [1]. Various higher order circumferential modes have been extensively studied in the previous reports regarding ring- or disk-shaped USMs [9], [10]. However, high-order vibration modes along the vertical directions have rarely been reported. This study focuses on a high-order symmetric vibration mode in the vertical direction. As depicted in Fig. 1(c), the high-order mode has six vertical nodal lines, which also exist in the conventional third-order

---

Manuscript received November 6, 2017; accepted January 3, 2018. Date of publication January 16, 2018; date of current version April 16, 2018. Recommended by Technical Editor J. Shan. This work was supported by the Adaptable and Seamless Technology Transfer Program, A-step, from the Japan Science and Technology Agency, under Grant AS2711904S. The work of J. Wu was supported by a Grant-in-Aid for the Japan Society for the Promotion of Science Research Fellows under Grant 17J05057. *(Corresponding author: Jiang Wu.)*

The authors are with the Laboratory for Future Interdisciplinary Research of Science and Technology, Tokyo Institute of Technology, Yokohama 226-8503, Japan (e-mail: wujiang@sonic.pi.titech.ac.jp; ymizuno@sonic.pi.titech.ac.jp; knakamur@sonic.pi.titech.ac.jp).

Color versions of one or more of the figures in this paper are available online at http://ieeexplore.ieee.org.

Digital Object Identifier 10.1109/TMECH.2018.2794379

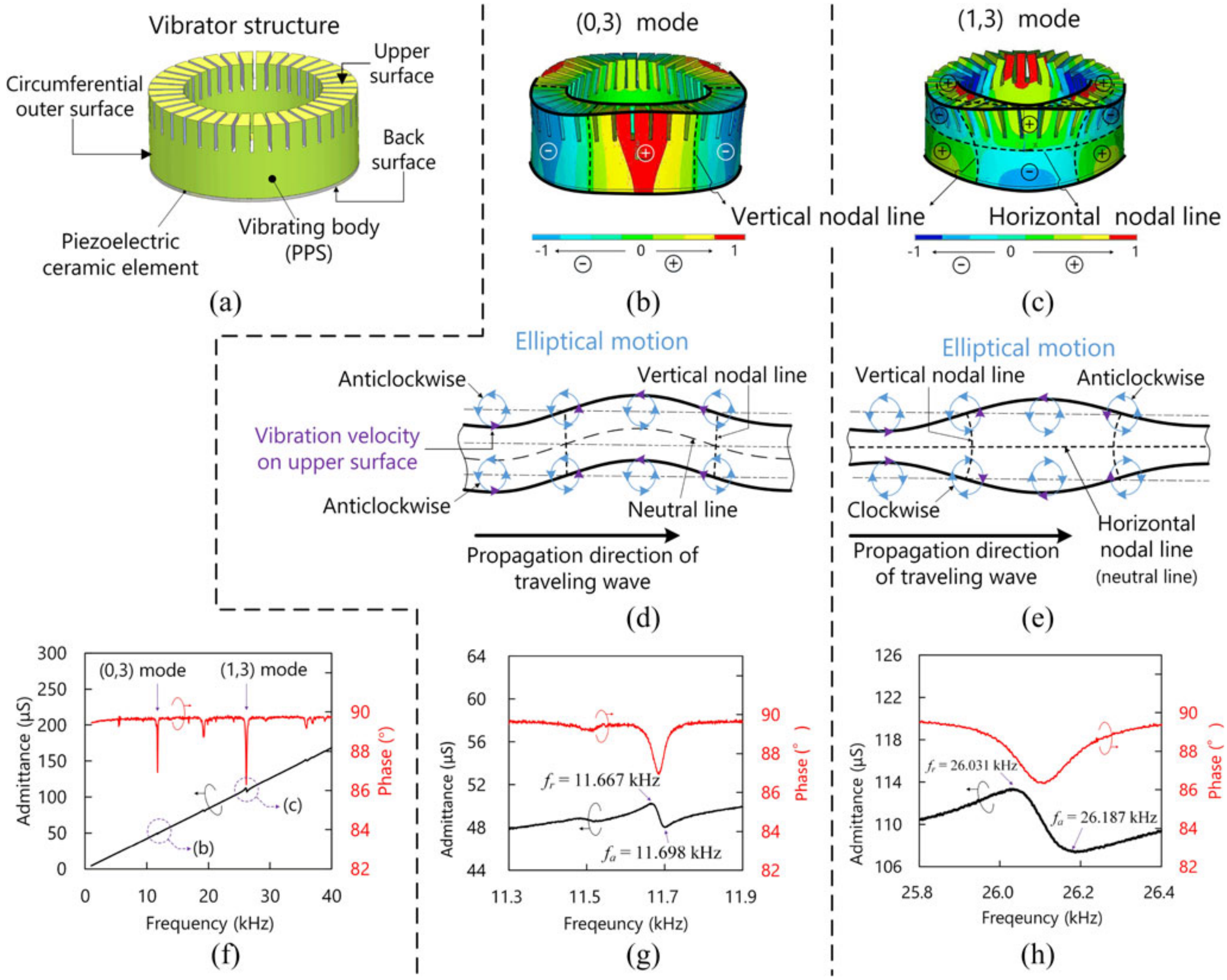

Fig. 1. Low- and high-order vibration modes in a PPS-based cylindrical vibrator and their admittance characteristics. (a) Structure of a vibrator, and (b) its admittance characteristics measured from 40 Hz to 40 kHz. (b) and (c) Show the vertical vibration velocity distributions in the (0, 3) and (1, 3) modes, respectively. As (d) shows, when a traveling wave in the (0, 3) mode propagates rightwards, the points located on both the upper and back surfaces have counter-clockwise elliptical motions. In contrast, the elliptical motions of points on the upper and back surfaces are anticlockwise and clockwise with the (1, 3) mode, respectively, as shown in (e). The admittance characteristics of the vibrator measured from 0.04 kHz to 40 kHz are shown in (f). In the ranges of 11.3–11.5 kHz, and 25.8–26.4 kHz, there are two observable responses, which corresponds to the (0, 3) and (1, 3) modes shown in (g) and (h), respectively. f_r and f_a represent the resonance and anti-resonance frequencies, respectively, using which, the electromechanical coupling factor can be calculated.

bending mode, but a horizontal nodal line on the circumferential outer surface of the vibrator. Many conventional traveling-wave USMs with ring or hollow-cylindrical shapes exhibit a significant deterioration in performance when their outer surfaces are fixed because there are no nodes with bending modes [1], [9], [16]. This problem may be solved by using the horizontal nodal line [17]. In addition, when the vibrator operates in the bending mode, as Fig. 1(d) shows, the points located on both the upper and back surfaces exhibit elliptical motions in identical directions. In contrast, when the vibrator is operated in the high-order mode, as Fig. 1(e) illustrates, the elliptical motions of the points on its upper and back surfaces have inversely rotational directions [18]. The admittance characteristics of the PPS-based vibrator shown in Fig. 1(f)–(h) demonstrate that the third bending and high-order modes are excited at approximately 11.7 and 26.0 kHz, respectively. The high-order mode has an electromechanical coupling factor of 1.4% (see Section III-B for its calculation method), relatively high compared to 0.4%, the value corresponding to the third bending mode, and it may result in relatively high output power of the PPS-based USM [19]. Here, we use (m, n) to represent a vibration mode, where m and n are respectively the orders of the vibration modes along the horizontal and vertical directions. Accordingly, the third bending mode and the high-order mode are referred to as the (0, 3) and (1, 3) modes, respectively [18]. Though the vibration performance of the (1, 3) mode was evaluated in a metal hollow rod [20], its application to USMs was not systematically examined [21].

In this study, first, we investigate the basic vibration characteristics of the polymer-based vibrators with the (1, 3) modes. Subsequently, we assess the performance of the motors with

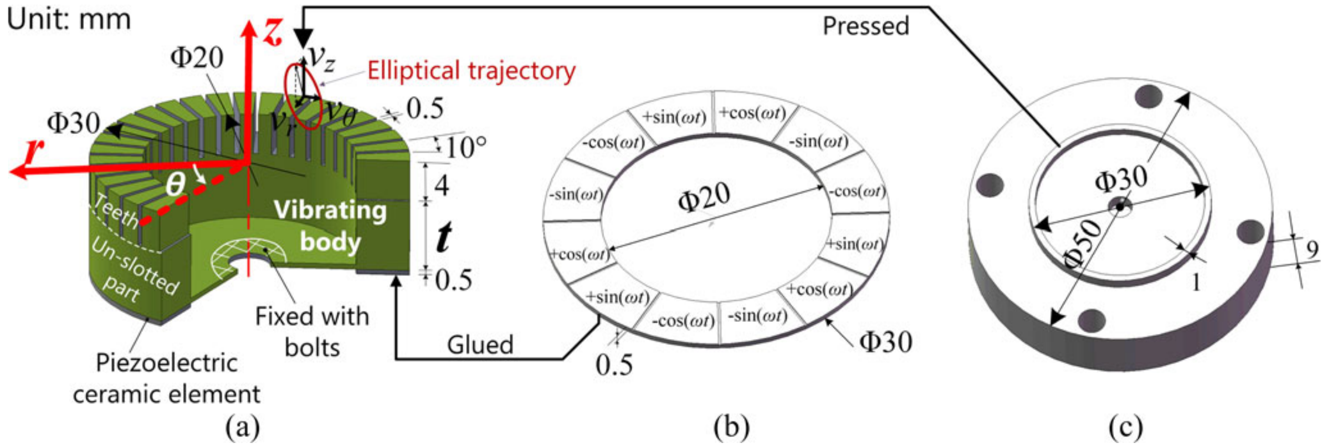

Fig. 2 Schematic of PPS-based USM. (a) Vibrating body, (b) annular piezoelectric ceramic disk, and (c) rotor. v_z, v_θ, and v_r denote the vibration velocities along the vertical (*z*), circumferential (*θ*), and radial (*r*) directions, respectively. They form an elliptical trajectory when a traveling wave propagates on the vibrator.

TABLE I
MECHANICAL CONSTANTS

Material	Elastic modulus (GPa)	Density ($\times\ 10^3$ kg/m^3)	Poisson's ratio
PPS	3.45	1.35	0.36
Stainless steel	197	7.9	0.29

the (1, 3) modes and make comparisons with other motors. Finally, we discuss why the (1, 3) and (0, 3) modes are optimal for polymer-based and thin metal-based motors, respectively, on the basis of their basic vibration characteristics.

II. CONFIGURATION OF PPS-BASED VIBRATOR

Fig. 2(a) illustrates the detailed configuration of the vibrator, which incorporates a PPS vibrating body and an annular piezoelectric ceramic disk. The vibrating body comprises a cylindrical part with outer and inner diameters of 30 and 20 mm, respectively, and a back disk with a thickness of 0.5 mm. Slots with 4-mm depths and 0.5-mm widths are introduced at 10° intervals on the cylindrical part. The thickness of the unslotted part, *t*, is varied, and its effects on the motor performance are explored in the following sections. A central hole is created on the back disk to fix the vibrator. The mechanical constants of PPS are summarized in Table I. A polar coordinate system (*z*-, *θ*-, and *r*-axes) is established on the upper surface. The piezoelectric ceramic disk (C213, Fuji Ceramics, Fujinomiya, Japan) has outer and inner diameters of 20 and 30 mm, respectively, and a thickness of 0.5 mm. One side of the sliver electrode is evenly divided into 12 parts, of which the polarization directions are identical and the undivided side is glued onto the back surface of the vibrating body with epoxy resin. As shown in Fig. 2(b), four channels of voltages with phase difference of 90° are applied to the electrodes. Thus, along the circumferential direction, the third-order bending mode is excited. The rotor depicted in Fig. 2(c) consists of a thin contact rim (30-mm outer and 28-mm inner diameters) and a flywheel (9-mm thickness and 50-mm diameter). In this study, the vibration velocity distribution on the upper surface of the vibrator is not considered because the rotor is in contact with the outer edge.

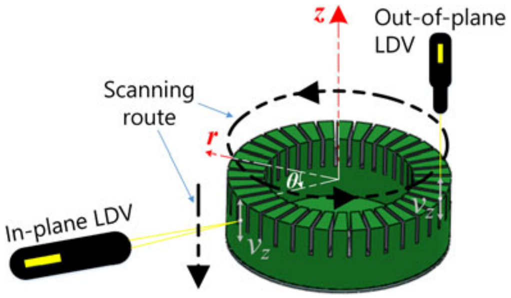

Fig. 3. Experimental setup for measuring *z*-axis vibration velocity distributions along circumferential and top surfaces. LDV: laser Doppler vibrometer.

III. (1, 3) VIBRATION MODE

A. Vibration Velocity Distribution

First, two voltages with a phase difference of 180°, amplitudes of 50 V, and frequency of 26.35 kHz were applied to generate a standing wave in the (1, 3) mode on the PPS-based vibrator with a 7-mm-thick unslotted part (t7 vibrator). As shown in Fig. 3, the *z*-axis vibration velocity was scanned along the vertical direction using an in-plane laser Doppler vibrometer (IPV100, Polytec, Waldbronn, Germany), and its amplitude *A* and the phase ϕ between the vibration velocity and input signal (as a reference signal) were recorded with a lock-in voltmeter (5560, NF Electronic Instruments, Yokohama, Japan). The sampling interval was set to 1 mm. The *z*-axis vibration velocity distribution on the outer edge of the upper surface was scanned along the circumference using an out-of-plane laser Doppler vibrometer (CLV1000, Polytec, Waldbronn, Germany). The sampling interval was set to 10° (one point per tooth). Fig. 4(a) illustrates that, as *z* ranged from 0 to –5 mm, the amplitude of the *z*-axis vibration velocity decreased from 52 to 3 mm/s and the phases were approximately 15°, while the amplitude increased from

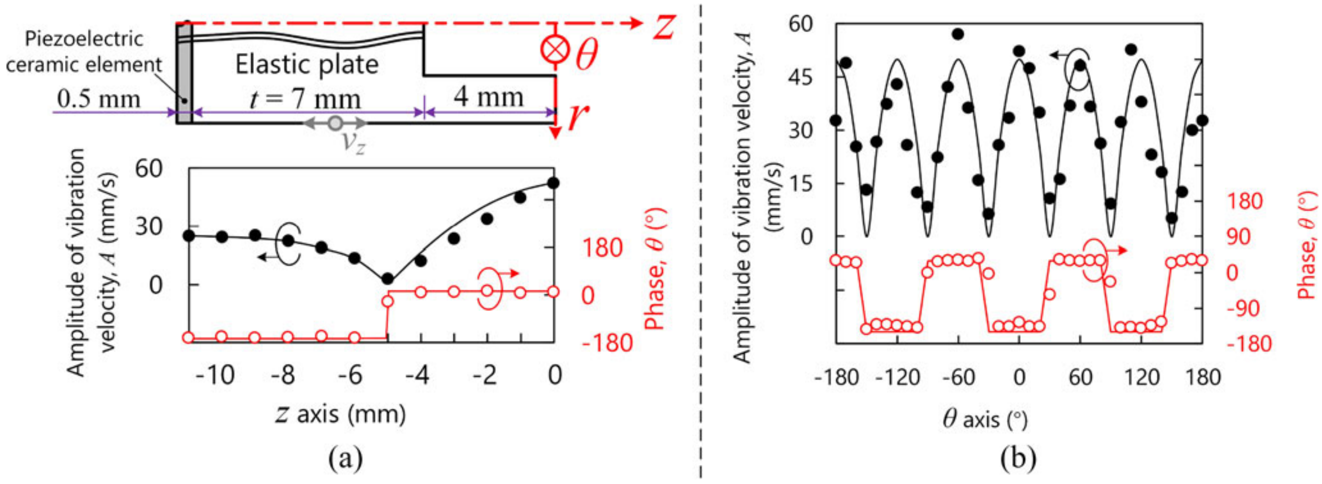

Fig. 4. Distributions of *z*-axis vibration velocities on the (a) circumferential outer surface and (b) upper surface.

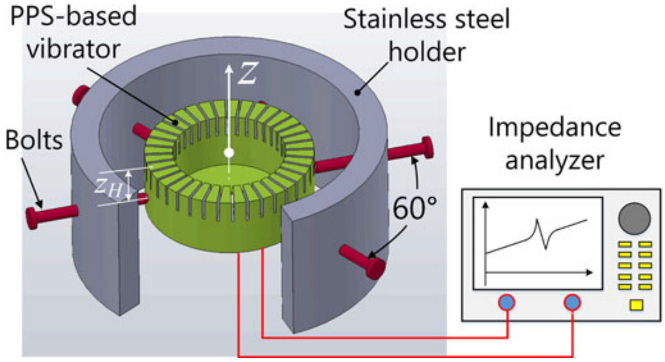

Fig. 5. Testbed for measuring admittance characteristics of vibrator with varying holding position.

3 to 25 mm/s, and the phases were –160° as z was decreased from –5 to –11 mm. Fig. 4(b) illustrates that three crests and three troughs appear on the outer edge of the upper surface. Clearly, the (1, 3) mode is successfully excited on the vibrator. Subsequently, to verify whether the vibrator can be fixed with low vibration loss by clamping its outer surface, we assessed the vibrator performance when the holding position z_H was changed. Fig. 5 depicts the testbed. The outer surface was tightly held with six bolts that are evenly distributed along the circumference of a stainless steel holder. From the admittance characteristics measured with an impedance analyzer (4294A, Agilent, Santa Clara, CA, USA), the mechanical quality factor (Q factor) is estimated using the following equation [15], [23] :

$$Q = \frac{f_r}{\Delta f} \tag{4}$$

where f_r and Δf represent the resonance frequency and the bandwidth corresponding to 0.707 times the peak amplitude, respectively. Table II lists the results. Clearly, the resonance-frequency variation and the Q-factor reduction at $z_H = -5$ mm, where the horizontal nodal line is located, are smaller than the values at $z_H = -2$ and –10 mm.

TABLE II
VIBRATION PERFORMANCE FOR VARIOUS HOLDING POSITIONS

Holding position, z_H (mm)	Resonance frequency, f_r (kHz)	Mechanical quality factor, Q
Without holder	25.857	182
–2	25.433	64
–5	25.833	159
–10	25.244	60

B. Changes in (1, 3) Vibration Mode With Thickness of Unslotted Part

By implementing finite element analysis (FEA), we explored how the (1, 3) mode changed as the thickness of the unslotted part was varied. Fig. 6(a)–(c) demonstrate the z-axis vibration velocity distributions on the t3, t7, and t10 vibrators, respectively. The horizontal nodal curve appears on the back disk of the t3 vibrator, and on the circumferential outer surface of the t7 vibrator. As depicted in Fig. 6(d), the bilateral sides of the teeth near the vertical nodal lines vibrate out of phase by 180°. Conversely, in the case of the t10 vibrator, the horizontal nodal line disappears, and all teeth yield out-of-phase vibration velocities. To verify whether these vibration modes were excited on teeth, the vibration velocity distributions of the t8 and t10 vibrators were measured in a period along the circumference (120°). The voltages applied to the vibrators were 150 V. Here, the sampling interval was set to approximately 1.6° (i.e., five points per tooth). The vibration velocity v_z plotted in Fig. 7 is calculated from its amplitude A and phase ϕ as follows:

$$v_z = A \cdot \mathrm{sgn}\left[\tan\left(\phi\right)\right] \tag{5}$$

where sgn donates the sign function. Fig. 7(a) shows that a cosine waveform was generated on the t8 vibrator, and among the 12 scanned teeth, the out-of-phase vibration velocities were observed on 6 teeth. When the unslotted part thickness increases to 10 mm, as Fig. 7(b) shows, out-of-phase vibration velocities are observed on all teeth. This mode is undesirable for USMs.

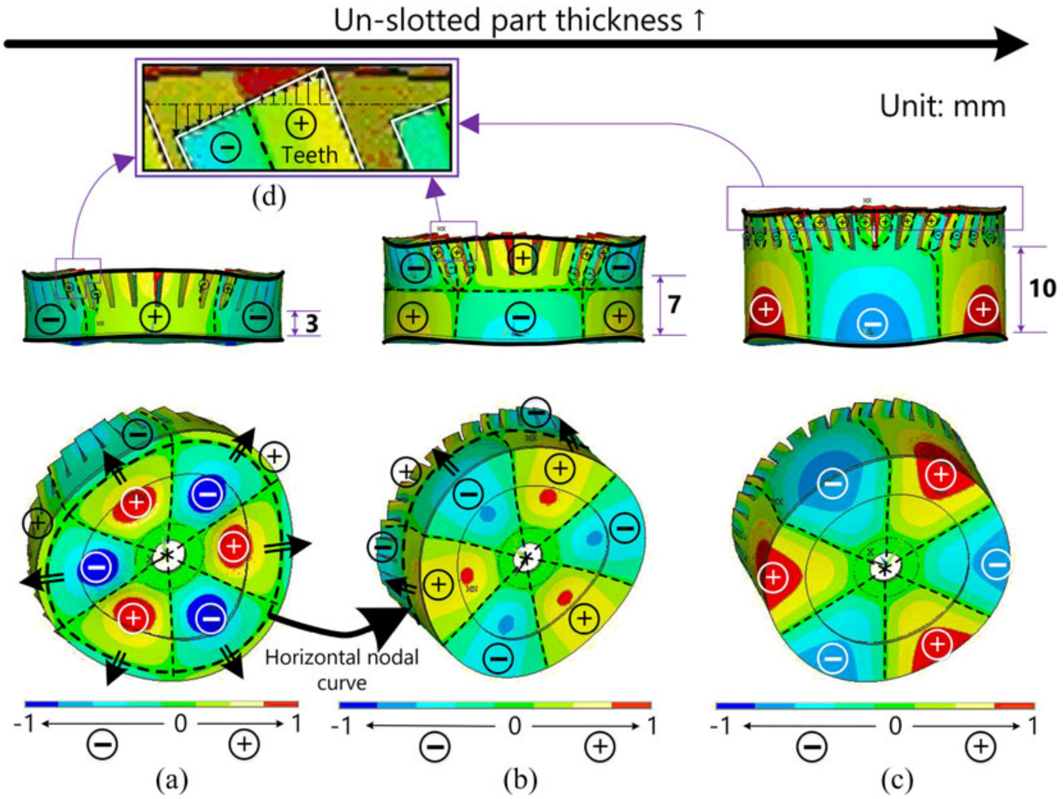

Fig. 6. (1, 3) bending modes on PPS-based vibrators with (a) 3-, (b) 7-, and (c) 10-mm-thick unslotted parts. The black dashed curves are the nodal lines located on the circumferential outer surfaces and the bottom surfaces. (d) shows a small scale view of the teeth near the top surface, where 180° out-of-phase vibration velocities are observed. The color legends indicate the *z*-axis vibration velocities.

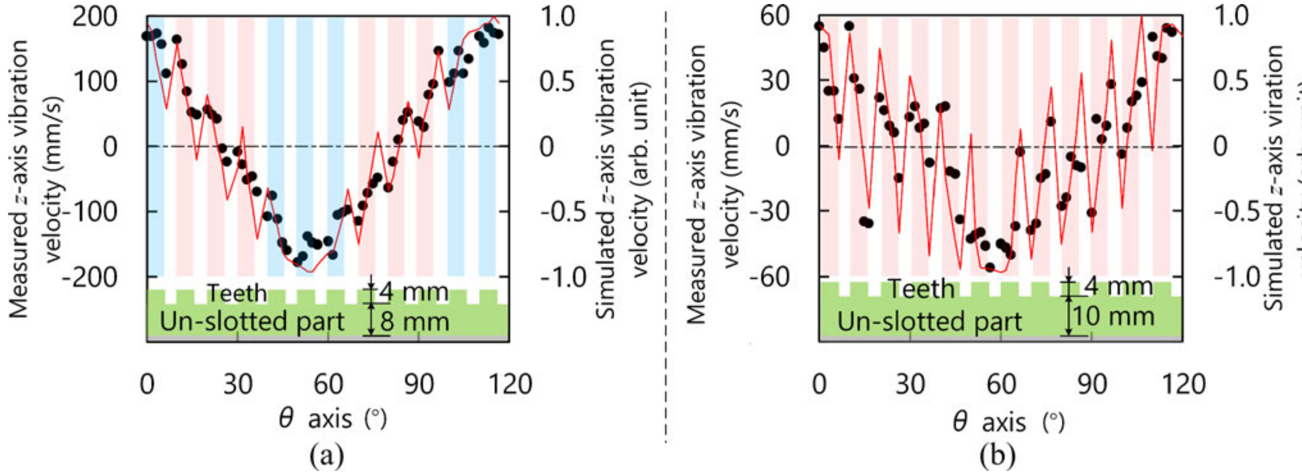

Fig. 7. Circumferential *z*-axis vibration velocity distributions on top surfaces of (a) t8 and (b) t10 vibrators. The dots represent the measured vibration velocities, and the lines represent the normalized vibration velocities calculated by FEA. The red and blue blocks represent the teeth with and without 180° out-of-phase vibration velocities, respectively.

Several points on the upper surface of the vibrator with relatively high vibration velocities drive the rotor, but most of the points, particularly those vibrating out of phase by 180°, generate slips with the rotor, which lead to friction loss and consequently low output torque and power [10]. The radius of the nodal circle, position of the nodal line, and ratio of the number of the teeth with 180° out-of-phase vibration velocities to the total number of teeth ($n_{\mathrm{in}} / n_{\mathrm{tot}}$) are plotted in Fig. 8 as functions of the unslotted part thickness. When the thickness of the unslotted part is less than 3.8 mm, a nodal circle, of which the radius increases as the vibrator becomes thicker, is located on the back surface. When the thickness ranges between 3.8 and 8.0 mm, the horizontal nodal line is located on the circumferential outer surface, and advances upward along the z-axis. The ratio $n_{\mathrm{in}} / n_{\mathrm{out}}$ increased from 50% to 100% as the unslotted part thickness varied from less than 8 to 10 mm.

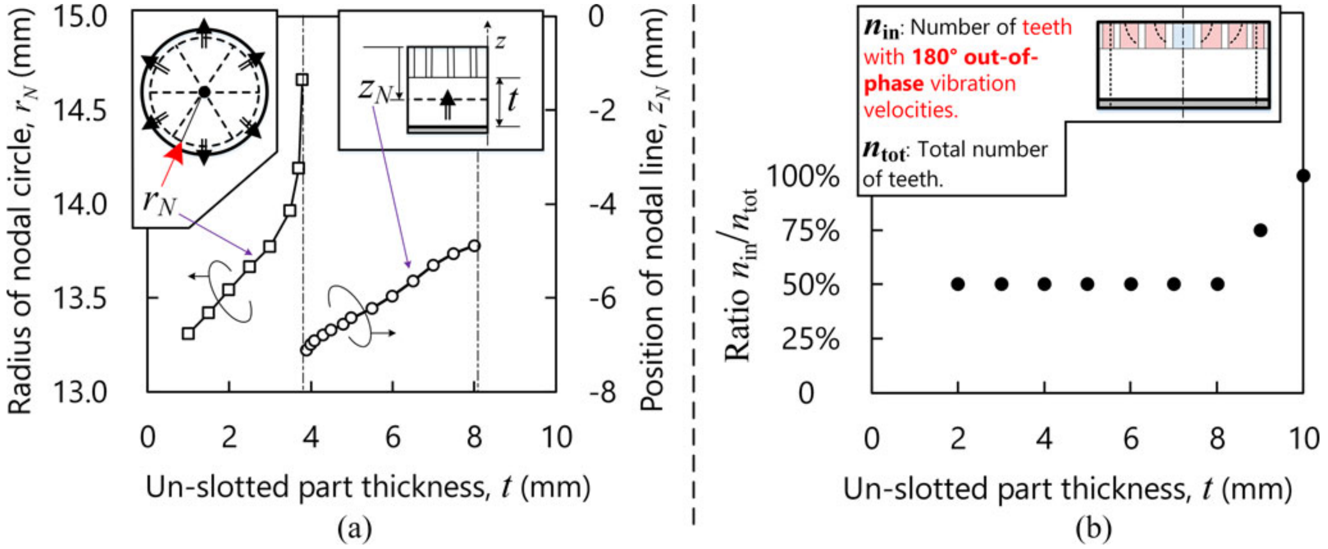

Fig. 8. (a) Radius of the nodal circle on bottom surface, r_N, and position of the horizontal nodal curve, z_N, on circumferential outer surface. (b) Ratio n_{in} / n_{tot} as a function of unslotted part thickness of the PPS-based vibrator with the (1, 3) mode.

Next, we investigated the basic vibration characteristics of the vibrators with varying thickness. The effective electromechanical coupling factor k_{eff}^2 is estimated from the resonance frequency f_r and the antiresonance frequency f_a [18], [22] as follows:

$$k_{\text{eff}}^2 = 1 - \left(\frac{f_r}{f_a}\right)^2. \tag{6}$$

The vibration velocity ratios, v_θ/v_z and v_r/v_z, show the elliptical motion shapes, which are important indicators for USMs [1], [2]. Here, v_z, v_θ, and v_r were measured at the antinode, node, and antinode, respectively. The force factor is defined as the ratio of the current to the vibration velocity, or equivalently the ratio of the generated force to the driving voltage [4], and it significantly affects the output torques of USMs [2], [24]. In this study, we investigated the ratio i/v_θ as the force factor because v_θ is parallel to the rotational direction. As Fig. 9(a) shows, the resonance frequency monotonically decreases from 27.15 to 25.91 kHz, and the electromechanical coupling factor increases from 1.3% to 1.5% as the unslotted part thickness increases from 5 to 10 mm. Fig. 9(b) shows that the ratio v_θ/v_z exhibits negligible variation, whereas the radial vibration components (v_r/v_z), which never contribute to the rotation of USMs [4], [17], increase rapidly. The force factor, as shown in Fig. 9(c), becomes higher with increasing thickness.

IV. MOTOR PERFORMANCE

A. Case Study

The testbed for estimating the motor performance is illustrated in Fig. 10 [4]. The vibrator was clamped to a stainless-steel shaft fixed to a stainless-steel base plate. A pivot bearing composed of a conical head and a dent was used to decrease the friction loss between the shaft and the rotor. The cone angles of the bearing head and the dent were 55° and 60°, respectively. The upper shaft of the bearing was inserted into a Teflon sleeve. The dent was fixed at the center of the rotor. The preload to the rotor was adjusted by varying the weights loaded on the top of the shaft.

Fig. 11 shows an example to demonstrate how the motor performance is estimated by the transient method [24], [25].

1) When the voltages were applied to the motor, the transient response of the rotational speed was measured using the two laser Doppler vibrometers [26]. Two beams illuminated a single point on the outer surface at identical angles, and the rotational velocity was calculated from the vibrometer outputs. The gray curve shown in Fig. 11(a) illustrates the transient response of the motor with the t8 vibrator when voltages of 250 V and a preload of 4.1 N are applied. After driving voltages were applied at approximately 8 ms, the rotational speed initially yielded a rapid increase, but the rotational acceleration decreased. At approximately 50 ms, the rotational speed gradually approached saturation, and then began fluctuating because of irregularities in assembly. The cutoff frequencies of the vibrometers were set to 0.2 and 100 kHz. Thus, the obtained curve transient response contained the ultrasonic vibration component, which should be the high-frequency fluctuation in this curve.
2) Exponential fitting (dashed curve) has been commonly implemented in previous studies [24], [25], assuming that rotational speeds of motors linearly decrease as their output torques become higher. However, in general, the load characteristics of motors are not perfectly linear. Thus, we employed the polynomial fitting $\varphi(t)$ [see the solid curve in Fig. 11(a)] to accurately represent the rise curve of the transient response.
3) The instantaneous output torque and power were respectively calculated using the following equation:

$$T(t) = J \cdot \frac{d\left[\varphi(t)\right]}{dt} \tag{7}$$

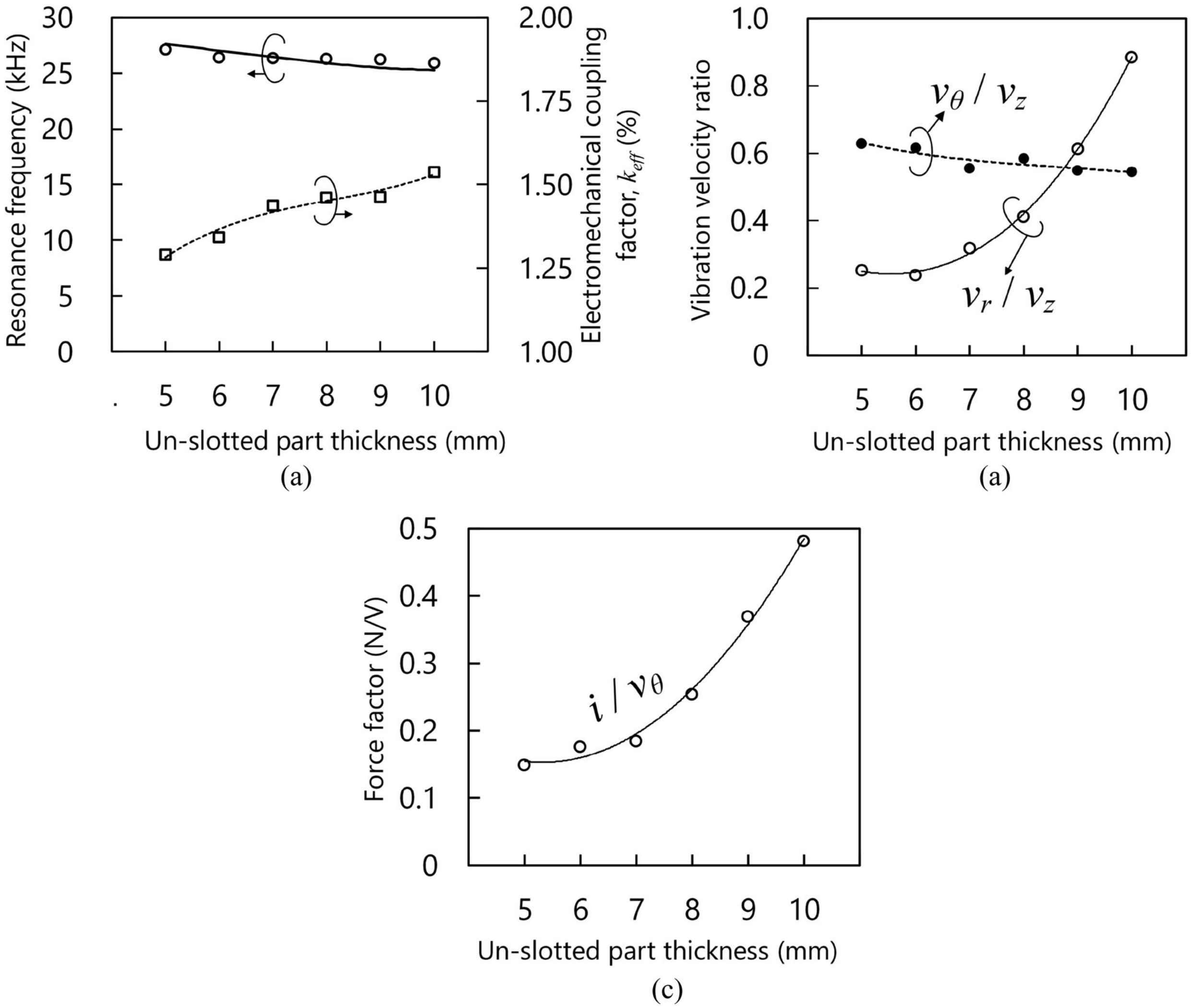

Fig. 9. Basic vibration characteristics of polymer-based vibrators with (1, 3) modes. (a) Resonance frequency and electromechanical coupling factor, (b) vibration velocity ratios, and (c) force factor as functions of unslotted part thickness.

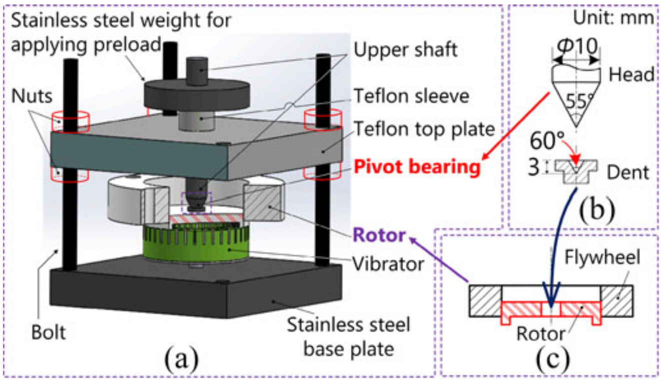

Fig. 10. Testbed for estimating motor performance: (a) Main body; (b) pivot bearing; and (c) rotor and flywheel.

and

$$P(t) = J \cdot \frac{d\left[\varphi(t)\right]}{dt} \cdot \varphi(t) \tag{8}$$

where J denotes the moment of inertia of the aluminum rotor, and equals 1.24×10^{-5} kg·m^2. The load characteristics shown in Fig. 11(b) were obtained from the rise part of the transient response. The maximum torque reached 4.5 mNm when the rotational speed equaled zero, and the maximum rotational speed was 7.7 rad/s when the rotor stopped accelerating. A maximum output power of approximately 10.6 mW was achieved when the motor yielded a moderate torque.

Fig. 12 demonstrates the motor performance with the (1, 3) mode as a function of the driving voltage when different preloads are applied to the motor with the t8 vibrator. Fig. 12(a) showed that, when the driving voltage was below 100 V, there were dead regions because of friction loss. Then, the maximum torque increased proportionally with increasing voltage, and leveled off at a certain voltage because it was limited by the preload [2], [4]. The maximum torque at 250 V reached 9.2 mNm when an optimal preload of 9.1 N was applied. As shown in Fig. 12(b), the no-load speed was approximately 12 rad/s at 250 V with a preload of 0.7 N. Fig. 12(c) demonstrated that, as the preload increased, the output power initially increased owing to the

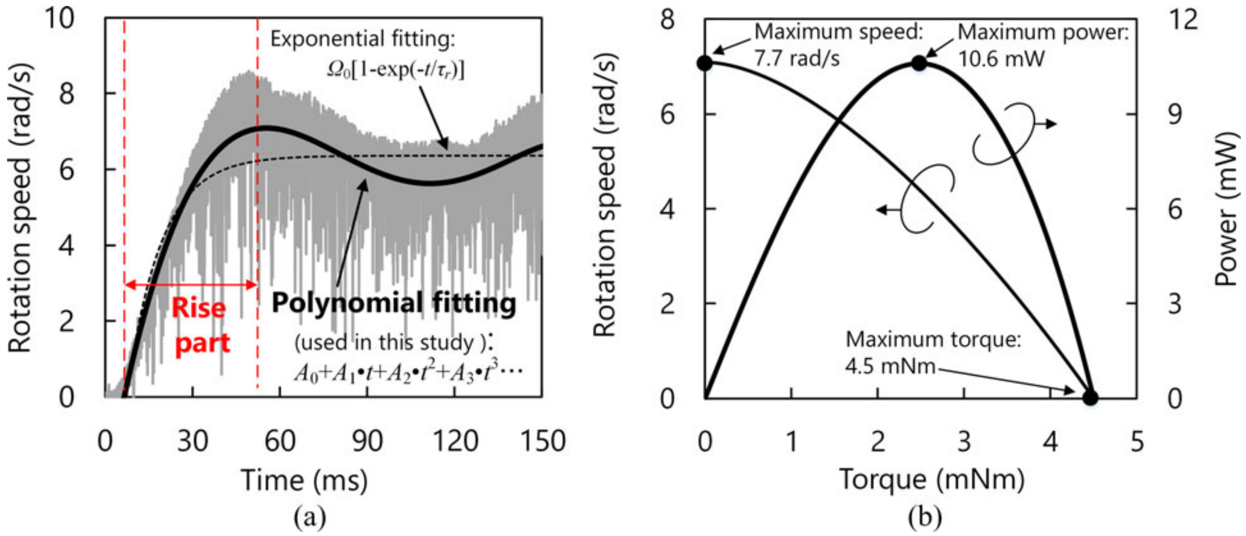

Fig. 11. (a) Transient response (gray curve) of PPS-based motor with t8 vibrator at voltages of 250 V voltages and a preload of 4.1 N. By polynomially fitting the rise part of the transient response curve. (b) The load characteristics are obtained.

increasing output torque, and then decreased when the preload increased beyond a certain value because of the reduction in the rotation speed. The motor yielded its maximum power of 10.9 mW when an optimal preload 6.4 N was applied to the t8 vibrator.

B. Performance of Motors With Varying Unslotted Part Thickness

Fig. 13(a)–(c) show the maximum torques, no-load speeds, and output powers and efficiencies, respectively, when voltages of 250 V are applied to motors with varying unslotted part thicknesses. Their performance was assessed at three random different positions. When the unslotted part thickness ranged from 5 to 7 mm, the maximum torque became higher because of the increase in the force factor [2], [4]. The no-load speeds have negligible variation because the tangential vibration velocities of the vibrators have almost no changes [10]. The output power became higher owing to the increasing electromechanical coupling factor. The motor with the t7 vibrator exhibited the highest output torque, power, and efficiency. When the unslotted part thickness exceeded 7 mm, the output torque, no-load speed, and output power exhibited rapid reductions, which can be qualitatively explained from the vibration characteristics. Owing to the aforementioned tangential vibration components opposing the rotational direction and the radial vibration components, the frictional loss tends to be high when the motors have thicker vibrators. Its negative effect on the output power offsets the positive effect caused by the increasing electromechanical coupling factors. Thus, the motor performance deteriorates when the vibrators are thicker than 7 mm.

Table III compares the performance of the PPS-based motors with (1, 3) and (0, 3) modes. The motor operating in the (1, 3) mode has a higher output torque, and the optimal thickness of its vibrator is lower than that with the (0, 3) mode. A relatively high rotational speed is obtained on the motor with a thin vibrator when the (0, 3) mode is excited. Owing to the higher electromechanical coupling factor, the motor operating in the (1, 3) mode has the maximum output power of 14.5 mW, 4.8 times the value with the (0, 3) mode. The power density, defined as the ratio of the output power to the vibrator weight, is also higher for the (1, 3) mode. As predicted, higher output torques and powers are achieved in the polymer-based motors by utilizing the high-order mode. However, the motors operating in the (1, 3) modes exhibited relatively low efficiencies, which are assumed to be dominantly caused by the aforementioned 180° out-of-phase vibration velocities. Note that, owing to the low stiffness, the teeth easily generate bending vibration (while the unslotted part does not oscillate), lowering the efficiencies of motors particularly when they have large depths. However, the FEA results demonstrate that, in the cases of our tested motors, the resonance frequencies corresponding to the bending vibration on the slots are in the range 22–24 kHz, deviating from the values for the (1, 3) modes. It allows us to infer that the tooth vibration has negligible influence on the motor performance. Additionally, our previously tested polymer-based vibrators with the low-order modes were operable in an audible frequency range owing to low elastic moduli of polymers [15]. By utilizing the high-order mode, the noise problem has been solved.

C. Comparison Between Polymer- and Metal-Based Motors Working With (1, 3) Modes

First, for comparison, the basic vibration characteristics of stainless-steel-based cylindrical vibrators with the (1, 3) modes were investigated through FEA. The adequate unslotted part thickness to generate a horizontal nodal line on the circumferential outer surface of the stainless-steel-based vibrator is 15 mm, which exceeds the practically applicable thickness of cylindrical vibrators [1], [10]. Two stainless-steel-based vibrators with 4- and 15-mm-thick unslotted parts (st4 and st15 vibrators, respectively) were fabricated.

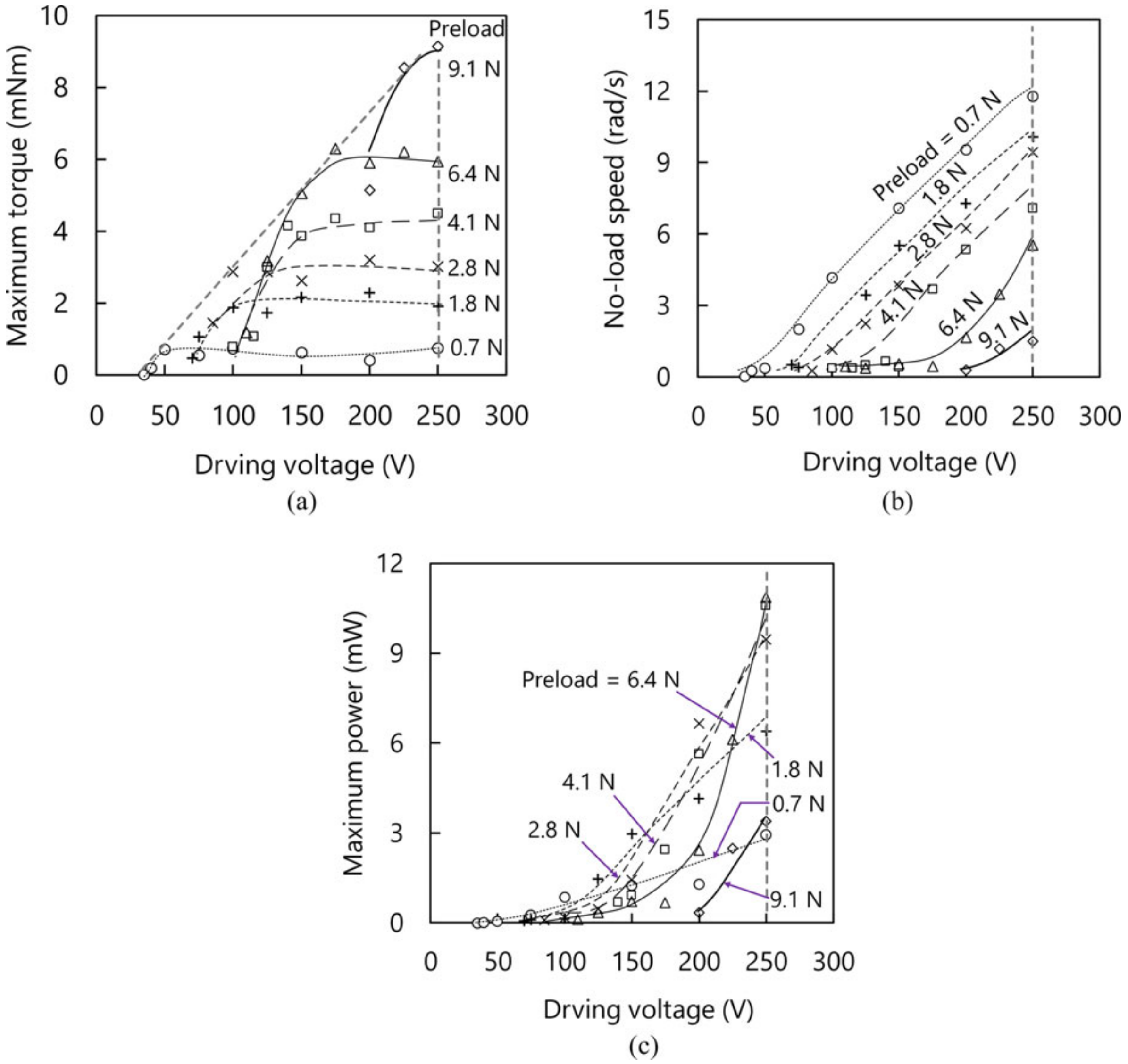

Fig. 12. Performance of USM with the t8 vibrator. (a) Maximum torque, (b) maximum no-load speed, and (c) maximum power versus driving voltage under different preloads.

The equivalent electrical circuit shown in Fig. 14 is a typical model for indicating the vibration characteristics [1], [2], [19], [23]. The circuit parameters of the polymer-based t5 and t7 vibrators and stainless-steel-based st4 and st15 vibrators are listed in Table IV. Clearly, when operating in the (1, 3) modes, the PPS-based vibrators exhibit relatively low equivalent masses and stiffnesses, resulting in relatively high electromechanical coupling factors and consequently high output powers. In contrast, the equivalent stiffness and mass of the stainless-steel-based st4 vibrator are lower when it operates in the (0, 3) mode. Their optimal modes are different possibly because of the difference in mechanical constants between the vibrating body (PPS, stainless steel) and excitor (piezoelectric ceramics) [4]. For the st15 vibrator, a lower equivalent stiffness and mass are obtained with the (1, 3) mode, but they are larger than the values of the PPS-based vibrators because of not only higher elastic modulus and density of stainless steel (see Table I) but also its high thickness.

Subsequently, the st4 and st15 vibrators are employed to form motors. To obtain a similar frictional condition, a 0.1-mm-thick PPS film was glued on the top surfaces. The performance of the stainless-steel-based motors is summarized in Table V. The high electromechanical coupling factor of the st4 vibrator with the (0, 3) mode leads to the high output power of the motor. Compared to the PPS-based motors with the (0, 3) mode, the motor provides a relatively high efficiency owing to its low mechanical loss [14], [16], but it cannot rotate with the (1, 3) mode. Though the motor with the st15 vibrator can rotate with the (1, 3) mode, it yields a relatively poor performance even when compared to the PPS-based motors. Undesirable tangential vibration components are also observed on all teeth, and the radial vibration component is very large for the st15 vibrator.

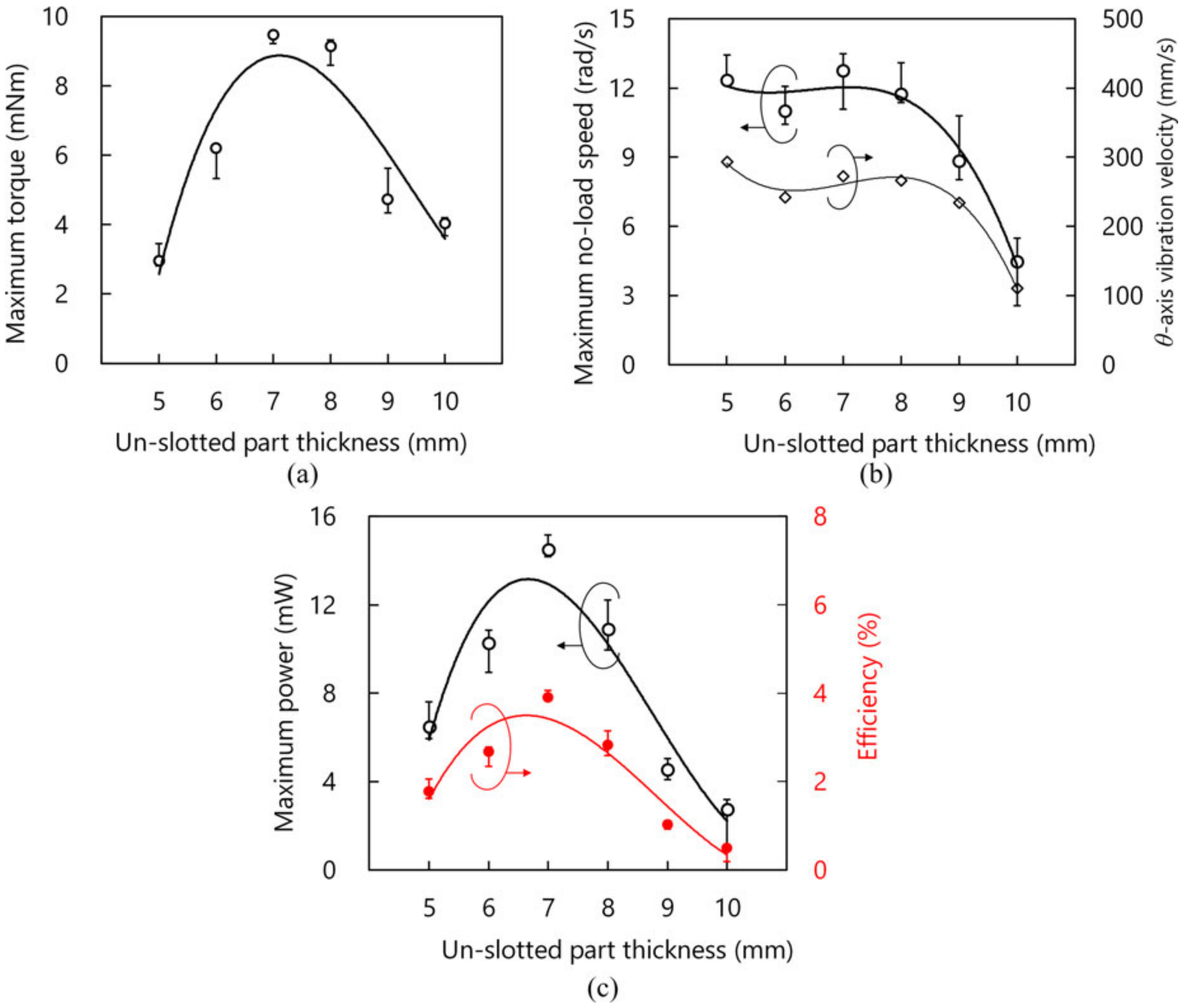

Fig. 13. Performance of USMs with varying unslotted part thickness. (a) Maximum torques at 250 V when optimal preloads are applied to vibrators, (b) no-load speeds under minimal preloads and tangential vibration velocities, and (c) maximum output powers and efficiencies.

TABLE III
POLYMER-BASED MOTOR PERFORMANCE WITH (1, 3) AND (0, 3) MODES

Performance at 250 V	(1, 3) mode	(0, 3) mode
Driving frequency (kHz)	25–27	7–13
Maximum torque (mNm)	9.5	2.9
Unslotted part thickness for maximum torque (mm)	7	8
Maximum rotational speed (rad/s)	12.3	16.1
Unslotted part thickness for maximum rotational speed (mm)	5–7	2
Maximum output power (mW)	14.5	3.0
Unslotted part thickness for maximum power (mm)	7	2
Maximum power density (W/kg)	5.8	2.5
Maximum efficiency	4.0%	4.8%

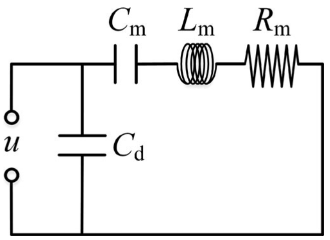

Fig. 14. Simplified equivalent circuit representing a piezoelectric transducer. C_d represents the clamped capacitance; and $1/C_m$, L_m , and R_m denote the equivalent stiffness, mass, and damper, respectively.

Finally, we compared the power densities between our polymer-based motors and several traveling-wave USMs reported in the last decade. Table VI indicates that our PPS-based motor with the (1, 3) mode provides relatively high power density. Additionally, its horizontal nodal line facilitates vibrator fixing. With these attractive advantages, our PPS-based motors are potentially applicable to driving lenses of cameras or optical instruments, where lightweights are required and moderate output power (or torques) are sufficient, but the fixing problem remains to be solved, though our current motors cannot provide better performance than some of the traveling-wave motors operating in more powerful modes [27]. It is also worth mentioning that, since PPS provides excellent chemical resistance [32], the

TABLE IV
MEASURED PARAMETERS OF EQUIVALENT CIRCUIT

Vibrator	Vibration mode	Clamped capacitance, C_d ($\times 10^{-12}$ F)	Equivalent stiffness, $1/C_m$ ($\times 10^{12}$ F^{-1})	Equivalent mass, L_m (H)	Equivalent damper, R_m ($\times 10^3$ Ω)
PPS-based t5 vibrator	(1, 3)	0.677	7.4	271.1	249.7
	(0, 3)	0.677	9.1	1963.6	591.2
PPS-based t7 vibrator	(1, 3)	0.676	5.0	188.1	163.6
	(0, 3)	0.668	10.1	1875.2	73.3
Stainless-steel-based st4 vibrator	(1, 3)	0.681	182.3	1039.0	970.9
	(0, 3)	0.681	0.5	19.3	6.6
Stainless-steel-based st15 vibrator	(1, 3)	0.684	61.2	181.9	224.1
	(0, 3)	0.683	102.4	1970.5	668.9

TABLE V
PERFORMANCE OF STAINLESS-STEEL-BASED VIBRATORS WITH (1, 3) AND (0, 3) MODES

Indicator		Vibrator with 4-mm-thick unslotted part		Vibrator with 15-mm-thick unslotted part	
		(1, 3) mode	(0, 3) mode	(1, 3) mode	(0, 3) mode
Vibrator performance	Driving frequency (kHz)	66.661	25.956	92.293	36.282
	Electromechanical coupling factor	0.1%	4.9%	0.5%	0.2%
Motor performance at 250 V	Maximum torque (mNm)	Stopped	20.8	0.8	Stopped
	Maximum rotational speed (rad/s)		10.8	1.4	
	Maximum output power (mW)		31.6	0.4	
	Power density (W/kg)		2.8	<0.1	
	Maximum efficiency		5.6%	0.7%	

TABLE VI
POWER DENSITIES OF RECENTLY REPORTED TRAVELING-WAVE USMS

Reference	Material of vibrating body	Excitation mode in piezoelectric ceramics	Power density (W/kg)
[27]	Stainless steel	d_{33} (longitudinal)	8.8
Our polymer-based motor	PPS	d_{31} (traverse)	5.8
[28]	Stainless steel	d_{31}	5.4
[29]	Stainless steel	d_{31}	4.8
[8]	Piezoelectric ceramics	d_{15} (shear)	4.3
[30]	Phosphorus bronze	d_{31}	3.1
[31]	Stainless steel	d_{31}	2.4

chemical industry would be a promising application area for our PPS-based motors.

V. CONCLUSION

This study presents the first report of the polymer-based USMs utilizing the (1, 3) mode. Through an investigation on the vibration characteristics and motor performance, we have drawn the following conclusions.

1) The (1, 3) mode introduced six vertical nodal lines and a horizontal nodal line on the circumferential outer surface of the polymer-based vibrator. It offers the advantage of fixing the vibrator without excessive vibration loss.
2) The PPS-based vibrator yields a higher electromechanical coupling factor with the (1, 3) mode than with the (0, 3) mode.
3) The optimal thickness of the PPS-based motor is lower with the (1, 3) mode than with the (0, 3) mode.
4) The maximum torque and power of the PPS-based motor utilizing the (1, 3) mode reached 9.5 mNm and 14.5 mW, respectively, higher than the values of both PPS-based motor using the (0, 3) mode and the stainless-steel-based motor using the (1, 3) mode.
5) The optimal modes for the PPS-based vibrators with practical thicknesses and stainless-steel-based thin vibrators are the (1, 3) and (0, 3) modes, respectively, because their equivalent stiffnesses and masses are relatively low when working in the optimal modes.

We have gained an understanding on the polymer-based USMs with the (1, 3) modes. In the future, the optimal design of the structures of vibrators, rotors, and accessory components will be investigated. In addition, the vibration modes will be explored in a wider frequency range to find the optimal ones (both in circumferential and vertical directions) to achieve practical applications of our polymer-based USMs.

ACKNOWLEDGMENT

The authors would like to thank the Daicel Corporation for providing the functional polymers, and the staff members of the Precision and Manufacturing Center, Technical Department, Tokyo Institute of Technology, for machining the motor components tested in this study.

REFERENCES

[1] S. Ueha and Y. Tomikawa, *Ultrasonic Motors—Theory and Applications*. New York, NY, USA: Oxford Univ. Press, 1993, ch. 1, pp. 4–13.
[2] K. Nakamura, M. Kurosawa, and S. Ueha, "Characteristics of a hybrid transducer-type ultrasonic motor," *IEEE Trans. Ultrason. Ferroelect. Freq. Control*, vol. 38, no. 3, pp. 188–193, May 1991.

[3] K. Takemura and T. Maeno, "Design and control of an ultrasonic motor capable of generating multi-DOF motion," *IEEE/ASME Trans. Mechatronics*, vol. 6, no. 4, pp. 499–506, Dec. 2001.

[4] J. Wu, Y. Mizuno, and K. Nakamura, "Structural parameter study on polymer-based ultrasonic motor," *Smart Mater. Struct.*, vol. 26, no. 11, 2017, Art. no. 115022.

[5] C.-H. Cheng and S.-K. Hung, "A piezoelectric two-degree-of-freedom nano-stepping motor with parallel design," *IEEE/ASME Trans. Mechatronics*, vol. 21, no. 4, pp. 2197–2199, Aug. 2016.

[6] Z. Zhu, S. To, K. F. Ehmann, and X. Zhou, "Design, analysis, and realization of a novel piezoelectrically rotary spatial vibration system for micro-/nanomachining," *IEEE/ASME Trans. Mechatronics*, vol. 22, no. 3, pp. 1227–1237, Jun. 2017.

[7] L. Yan, D. Liu, H. Lan, and Z. Jiao, "Compact traveling wave micromotor based on shear electromechanical coupling," *IEEE/ASME Trans. Mechatronics.*, vol. 21, no. 3, pp. 1572–1580, Jun. 2016.

[8] T. Mashimo, "Micro ultrasonic motor using a cube with a side length of 0.5 mm," *IEEE/ASME Trans. Mechatronics*, vol. 21, no. 2, pp. 1189–1192, Apr. 2016.

[9] N. W. Hagood and A. J. McFarland, "Modeling of a piezoelectric rotary ultrasonic motor," *IEEE Trans. Ultrason. Ferroelect. Freq. Control*, vol. 42, no. 2, pp. 210–224, Mar. 1995.

[10] H. Hirata and S. Ueha, "Design of a traveling wave type ultrasonic motor," *IEEE Trans. Ultrason. Ferroelect. Freq. Control*, vol. 42, no. 2, pp. 225–231, Mar. 1995.

[11] T. Mashimo, "Scaling of piezoelectric ultrasonic motors at submillimeter range," *IEEE/ASME Trans. Mechatronics*, vol. 22, no. 3, pp. 1238–1246, Jun. 2017.

[12] J. Li, X. Zhou, H. Zhao, M. Shao, N. Li, S. Zhang, and Y. Du, "Development of a novel parasitic-type piezoelectric actuator," *IEEE/ASME Trans. Mechatronics*, vol. 22, no. 1, pp. 541–550, Feb. 2017.

[13] J. Wu, Y. Mizuno, M. Tabaru, and K. Nakamura, "Measurement of mechanical quality factors of polymers in flexural vibration for high-power ultrasonic application," *Ultrasonics*, vol. 69, pp. 74–82, 2016.

[14] J. Wu, Y. Mizuno, M. Tabaru, and K. Nakamura, "Ultrasonic motors with polymer-based vibrators," *IEEE Trans. Ultrason. Ferroelect. Freq. Control*, vol. 62, no. 12, pp. 2169–2177, Dec. 2015.

[15] K. Nakamura, K. Kakihara, M. Kawakami, and S. Ueha, "Measuring vibration characteristics at large amplitude region of material for high power ultrasonic vibration system," *Ultrasonics*, vol. 38, nos. 1/2, pp. 122–126, 2000.

[16] R. Bansevičius, G. Kulvietis, and D. Mazeika, "Piezoelectric active bearings and supports: Structures, characteristics, and applications," *Arch. Appl. Mech.*, vol. 86, no. 10, pp. 120–126, 2016.

[17] M. Kurosawa, K. Nakamura, T. Okamoto, and S. Ueha, "An ultrasonic motor using bending vibrations of a short cylinder," *IEEE Trans. Ultrason. Ferroelect. Freq. Control*, vol. 36, no. 5, pp. 517–521, Sep. 1989.

[18] K. F. Graff, *Wave Motion in Elastic Solids*. New York, NY, USA: Dover, 1991, pp. 460–464.

[19] Y. Liu, W. Chen, J. Liu, and X. Yang, "A high-power linear ultrasonic motor using bending vibration transducer," *IEEE Trans. Ind. Electron.*, vol. 60, no. 11, pp. 5160–5166, Nov. 2013.

[20] H. Gravenkamp, C. Brik, and C. Song, "The computation of dispersion relations for axisymmetric waveguides using the scaled boundary finite element method," *Ultrasonics*, vol. 54, no. 5, pp. 1373–1385, 2014.

[21] A. Ukita and S. Ueha, "Hollow cylinder-shaped ultrasonic motor," [in Japanese], *J. Acoust. Soc. Jpn.*, vol. 44, no. 3, pp. 173–179, 1988.

[22] Q. Zhang, S. Shi, and W. Chen, "An electromechanical coupling model of a bending vibration type piezoelectric ultrasonic transducer," *Ultrasonics*, vol. 66, pp. 18–26, 2016.

[23] B. F. Ley, S. G. Lutz, and C. F. Rehberg, *Linear Circuit Analysis*. New York, NY, USA: McGraw-Hill, 1959, pp. 278–279.

[24] K. Nakamura, M. Kurosawa, H. Kurebayashi, and S. Ueha, "An estimation of load characteristics of an ultrasonic motor by measuring transient responses," *IEEE Trans. Ultrason. Ferroelect. Freq. Control*, vol. 38, no. 5, pp. 481–485, 1991.

[25] Q. Lv, Z. Yao, and X. Li, "Modeling and experimental validation of a linear ultrasonic motor considering rough surface contact," *Smart Mater. Struct.*, vol. 26, no. 4, 2017, Art. no. 045023.

[26] T. Shigematsu and M. K. Kurosawa, "Friction drive of an SAW motor. Part I: Measurements," *IEEE Trans. Ultrason. Ferroelect. Freq. Control*, vol. 55, no. 9, pp. 2205–2215, Sep. 2005.

[27] Y. Liu, W. Chen, J. Liu, and S. Shi, "A cylindrical traveling wave ultrasonic motor using longitudinal and bending composite transducer," *Sens. Actuators A*, vol. 161, nos. 1/2, pp. 158–163, 2010.

[28] W. Chen, S. Shi, Y. Liu, and P. Li, "A new traveling wave ultrasonic motor using thick ring stator with nested PZT excitation," *IEEE Trans. Ultrason. Ferroelect. Freq. Control*, vol. 57, no. 5, pp. 1160–1168, May 2010.

[29] T. Peng, H. Shi, X. Liang, F. Luo, and X. Wu, "Experimental investigation on sandwich structure ring-type ultrasonic motor," *Ultrasonics*, vol. 56, pp. 303–307, 2015.

[30] D. An, M. Yang, X. Zhuang, T. Yang, F. Meng, and Z. Dong, "Dual traveling wave rotary ultrasonic motor with single active vibrator," *Appl. Phys. Lett.*, vol. 110, 2017, Art. no. 143507.

[31] X. Yang, Y. Liu, W. Chen, and J. Liu, "A cylindrical traveling wave ultrasonic motor using bond-type composite beam," *Ultrasonics*, vol. 65, pp. 277–281, 2016.

[32] Chemical resistance of TORELINA (PPS products of TORAY). [Online] Available: http://www.toray.jp/plastics/en/toreline/technical/tec_022.html. Accessed on: Nov. 6, 2017.

Jiang Wu was born in Liaoning, China, on January 29, 1988. He received the B.E. degree in mechanical engineering from the Dalian University of Technology, Dalian, China, in 2010, the M.E. degree in mechatronic engineering from the State Key Laboratory of Robotics and System, Harbin Institute of Technology, Harbin, China, in 2012, and the Dr. Eng. degree in electrical and electronic engineering from the Future Interdisciplinary Research of Science and Technology, Tokyo Institute of Technology, Yokohama, Japan, in 2017.

His research interests include piezoresistive and piezoelectric materials, permanent-magnet-based sensing technology, and polymer-based ultrasonic transducers and actuators.

Yosuke Mizuno (M'14–SM'17) was born in Hyogo, Japan, on October 13, 1982. He received the B.E., M.E., and Dr. Eng. degrees in electronic engineering from the University of Tokyo, Tokyo, Japan, in 2005, 2007, and 2010, respectively.

From 2007 to 2010, he was involved in Brillouin optical correlation-domain reflectometry for his Dr.Eng. degree at the University of Tokyo. From 2007 to 2010, he was a Research Fellow (DC1) of the Japan Society for the Promotion of Science (JSPS). From 2010 to 2012, as a Research Fellow (PD) of JSPS, he worked on polymer optics with the Tokyo Institute of Technology, Yokohama, Japan. Since 2012, he has been an Assistant Professor with the Precision and Intelligence Laboratory (currently the Institute of Innovative Research), Tokyo Institute of Technology, Yokohama, Japan, where he is active in fiber-optic sensing, polymer optics, and ultrasonics.

Dr. Mizuno was the recipient of the Ando Incentive Prize for the Study of Electronics in 2011, the Tokyo Tech Challenging Research Award in 2013, the Konica Minolta Imaging Science Award in 2014, and the Japanese Society of Applied Physics (JSAP) Young Scientist Presentation Award in 2015. He is a member of the IEEE Photonics Society (Senior Member), JSAP, and the Institute of Electronics, Information, and Communication Engineers of Japan.

Kentaro Nakamura (M'00) was born in Tokyo, Japan, on July 3, 1963. He received the B.E., M.E., and Dr.Eng. degrees from the Tokyo Institute of Technology, Yokohama, Japan, in 1987, 1989, and 1992, respectively.

Since 2010, he has been a Professor with the Precision and Intelligence Laboratory (currently the Institute of Innovative Research), Tokyo Institute of Technology. His research interests include applications of ultrasonic waves, measurement of vibration and sound using optical methods, and fiber-optic sensing.

Prof. Nakamura was the recipient of the Awaya Kiyoshi Award for Encouragement of Research from the Acoustical Society of Japan (ASJ) in 1996, and the Best Paper Awards from the Institute of Electronics, Information, and Communication Engineers (IEICE) of Japan in 1998 and from the Symposium on Ultrasonic Electronics in 2007 and 2011. He also received the Japanese Journal of Applied Physics Editorial Contribution Award from the Japan Society of Applied Physics in 2007. He is a member of the ASJ, the Japanese Society of Applied Physics, the IEICE, and the Institute of Electrical Engineers of Japan.